Results of aperture area comparisons for exo-atmospheric total solar irradiance measurements

B. Carol Johnson,[1,*] Maritoni Litorja,[1] Joel B. Fowler,[1] Eric L. Shirley,[1] Robert A. Barnes,[2] and James J. Butler[3]

[1]National Institute of Standards and Technology, Gaithersburg, Maryland 20899, USA

[2]Science Applications International Corporation, Beltsville, Maryland 20705, USA

[3]National Aeronautics and Space Administration, Goddard Space Flight Center, Greenbelt, Maryland 20771, USA

*Corresponding author: cjohnson@nist.gov

Received 10 July 2013; accepted 18 August 2013;
posted 24 September 2013 (Doc. ID 193644); published 13 November 2013

Exo-atmospheric solar irradiance measurements made by the solar irradiance community since 1978 have incorporated limiting apertures with diameters measured by a number of metrology laboratories using a variety of techniques. Knowledge of the aperture area is a critical component in the conversion of radiant flux measurements to solar irradiance. A National Aeronautics and Space Administration (NASA) Earth Observing System (EOS) sponsored international comparison of aperture area measurements of limiting apertures provided by solar irradiance researchers was performed, the effort being executed by the National Institute of Standards and Technology (NIST) in coordination with the EOS Project Science Office. Apertures that had institutional heritage with historical solar irradiance measurements were measured using the absolute aperture measurement facility at NIST. The measurement technique employed noncontact video microscopy using high-accuracy translation stages. We have quantified the differences between the participating institutions' aperture area measurements and find no evidence to support the hypothesis that preflight aperture area measurements were the root cause of discrepancies in long-term total solar irradiance satellite measurements. Another result is the assessment of uncertainties assigned to methods used by participants. We find that uncertainties assigned to a participant's values may be underestimated.

OCIS codes: (120.0280) Remote sensing and sensors; (120.3940) Metrology; (120.6085) Space instrumentation.

http://dx.doi.org/10.1364/AO.52.007963

1. Introduction

A. Motivation for the Measurement of Total Solar Irradiance

Radiant flux from the sun is the primary source of energy for the Earth. Photosynthesis, temperature, atmospheric, and oceanic dynamics, and the extent of the protective stratospheric ozone layer are all a function of exo-atmospheric solar irradiance. Solar irradiance monitoring is important for studies of global climate change, paleo-climatic studies, solar physics, and space weather. The solar radiant output is variable both spectrally and temporally on multiple time scales [1,2]. One measure of solar output is total solar irradiance (TSI), which is the radiant energy emitted by the sun over all spectral regions falling each second on 1 square meter outside the Earth's atmosphere and normalized to 1 astronomical unit from the sun.

For global climate change studies, long-term (decadal) changes in solar irradiance are of interest [3,4]. The absolute value of the TSI is necessary input to numerical climate models, and any long-term changes in solar irradiance must be understood in order to separate solar forcing on the Earth's climate from other natural phenomena and anthropogenic sources. For example, a recent model of the influence of solar irradiance, anthropogenic effects, El Niño southern oscillation, and ash from volcanic eruptions on global and regional surface temperatures was developed using historical empirical data and linear regression [5]. The solar irradiance increases about 0.1% from minimum to maximum during the 11 year solar cycle; this study concluded the sensitivity in global surface temperature was 0.1°C per 0.1% change in TSI. This is large enough to counteract or enhance the effects of anthropogenic forcing on the time scales of a solar cycle [6]. The question of long-term change, e.g., different values of TSI at different solar minima, is open. Quantification of long-term change will require space-based TSI measurements with combined uncertainties of less than 0.01% or continual measurements from temporally overlapping missions using instruments with radiometric stabilities better than 0.001%/yr [7].

B. Historical TSI Record from Space

Satellite instruments have typical on-orbit measurement lifetimes of five years. Therefore, continuous measurements of solar irradiance require multiple instruments. On-orbit measurements with various instruments have been acquired since the 1978 launch of the Earth Radiation Budget Experiment (ERBE) on Nimbus 7. Table 1 lists the past, current, and future long-term, TSI satellite instruments and their on-orbit measurement intervals. The historical TSI database produced from these measurements for several of the instruments in Table 1 is shown in Fig. 1 on their native scales. From the data in Fig. 1, the majority of the instruments have adequate precision to discern the 11 year solar cycle, and the measurements agree in the relative magnitude of the differences from minimum to maximum, but disagree by up to 10.5 W/m^2 (or about 0.8%) in TSI values at solar minimum. These differences in absolute level are several times the relative difference of 1.3 W/m^2 (0.1%) between solar maximum and minimum. The observed discrepancies introduce ambiguity in the absolute solar irradiance. Without adequate understanding of the source of the discrepancies, one is forced to choose a reference value when producing a continuous record of TSI from the data in Fig. 1. A primary difficulty in constructing the composite time series is the correction for sensor drift during a mission, especially when data gaps occur.

Table 1. Long-Term TSI Satellite Instruments and Associated Data Records from 1978 to the Present and Near Future[a]

Instrument or Experiment/ Platform	TSI Data Record
ERB, ERBE/Nimbus 7	Nov. 1978 to Dec. 1993
ACRIM I/SMM	Feb. 1980 to Jun. 1989
ERBE/ERBS	Oct. 1984 to Oct. 2005
ERBE/NOAA 9 Satellite	Jan. 1985 to Dec. 1989
ERBE/NOAA 10 Satellite	Oct. 1986 to Dec. 1987
ACRIM II/UARS	Oct. 1991 to Nov. 2001
SOVA/EURECA	Jul. 1992 to Jun. 1993
SOLCON/Spacelab 1, ATLAS and Hitchhiker (space shuttle)	Nov. 1983, Mar. 1992, Apr. 1993, Nov. 1994, Aug. 1997, Oct. 1998, Feb. 2003
VIRGO/SOHO	Dec. 1995 to present
ACRIM III/ACRIMSAT	Apr. 2000 to present
TIM/SORCE	Feb. 2003 to present
SOVIM/ISS	Feb. 2008 to Sept. 2008
SOVAP & PREMOS/PICARD	Jun. 2010 to present
TIM/GLORY	Launch Failure Mar. 2011
TCTE[b]/NASA/NOAA	Fall 2013 planned launch date
TSIS[b]/JPSS	Fall 2016 planned launch date

[a]The acronyms are defined in Appendix A.
[b]The TCTE and TSIS missions use the TIM instrument.

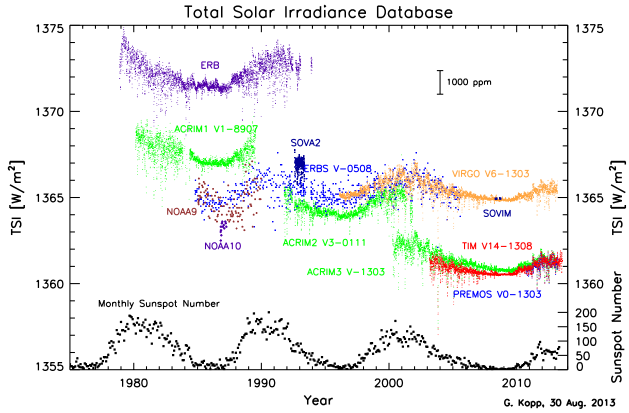

Fig. 1. TSI measurements made since 1978 along with the monthly sunspot number as of 30 August 2013 [8].

C. TSI Measurement Method and Philosophy

Measurements of TSI use electrical substitution radiometers, which determine optical power through a comparison with an equivalent amount of electrical power. Electrical substitution radiometers typically employ an absorptive cavity equipped with a heater and are coupled to a heat sink maintained at a constant reference temperature. Flux incident on the cavity induces a measured temperature rise in the cavity. The cavity is then shuttered from the incident solar flux, and electrical power to the cavity heater is increased to that level at which the cavity temperature is equal to that measured with the shutter open. The optical power, to a first approximation, is proportional to this electrical power increase and is given by the product of the increased heater current squared and the heater resistance [9]. In the measurement of TSI, electrical substitution radiometers are often equipped with multiple cavities employed as either primary measurement cavities or as backup or reference cavities used for trending on-orbit cavity degradation. The best results with electrical substitution radiometers are obtained with operation at cryogenic temperatures, but this is difficult in orbit, and the instruments are operated at ambient temperature.

Given that the measurement objective is to detect real changes in TSI over multiple solar cycles, two measurement philosophies are possible: (1) strive for absolute values of TSI in which the sensors are considered primary standards, requiring thorough characterization and calibration; or (2) strive for "the best" relative values of TSI in which the sensors are designed to be immune to any long-term, time-dependent biases that would affect the temporal record (e.g., sensor degradation); any necessary correction factors are then developed by the inclusion of additional measurements and/or measurement protocols.

If the satellite data sets do not overlap in time, absolute measurements with uncertainty of 0.01% are required, and an instrument must be temporally stable commensurate with its anticipated mission lifetime, e.g., $<0.001\%/\mathrm{yr}$ [7]; this is method 1. However, these uncertainty and stability goals are comparable to existing laboratory cryogenic radiometry. An international intercomparison of cryogenic radiometers using ≈1 mW lasers and silicon photodiode trap detectors as transfer standards revealed that National Metrology Institutes (NMI) measure optical power with uncertainty of 0.02% ($k = 2$) [10]. In addition, cryogenic radiometry was not available during the initial TSI studies, and only recently has a laboratory cryogenic radiometer been realized that is capable of flux and irradiance calibrations at solar levels of 68 mW with an aperture of 0.5 cm^2 [11]. As a consequence, system-level comparisons to laboratory cryogenic radiometers were considered to be at best a validation effort. Instead, substantial effort has been invested in the construction of the long-term data record from satellite sensors under the relative TSI measurement paradigm (method 2), but this requires continuous measurements in the form of multiple sensors on overlapping missions and an extremely thorough characterization of sensor performance. In particular, it is difficult to validate radiometric stability during the mission at the required level of 0.001%/yr level of degradation, leading to conflicting interpretations of the solar record [12].

D. Uncertainty in TSI Measurements

There are numerous sources of uncertainty in satellite TSI measurements. Uncertainties in aperture area or the on-board electrical standards enter into the TSI uncertainty budget in a direct fashion. The measured "raw" values must be corrected for a number of effects, such as signal contribution from thermal radiation due to solar heating of the cavity shutter when closed, diffraction, and scatter in the cavity optical subsystem. Finally, any temporal changes that may occur between preflight testing and first in-flight measurements and changes on various time scales during the mission, such as those due to degradation of the cavity absorptance or variations in the spacecraft orbit orientation must be considered, and the associated uncertainty in these corrections accounted for in the TSI uncertainty budget.

Comprehensive, realistic determination of the measurement uncertainties for either the absolute or relative TSI measurement philosophy is difficult. Early estimates are between 0.2% and 0.3% ($k = 1$) [12]. In an effort to examine the observed 0.35% discrepancy in the TSI record, which was evident once the total irradiance monitor (TIM) launched in 2003, a workshop hosted by the National Aeronautics and Space Administration (NASA) and the National Institute of Standards and Technology (NIST) was held in July 2005 at NIST to specifically address this issue [13]. At the time of launch, TIM's uncertainty in TSI values was estimated to be 0.01% [14], which was negligible in terms of the observed discrepancy. At the workshop, sources of uncertainty such as diffraction, scattered radiation, and background were presented and discussed. Preliminary results for the aperture comparison reported here were presented. Uncertainty budgets for the ERBE on the Earth Radiation Budget Satellite (ERBS), TIM on the Solar Radiation and Climate Experiment (SORCE), the Active Cavity Radiometer III (ACRIM III) on the Active Cavity Radiometer Irradiance Monitor SATellite (ACRIMSAT), and the DIfferential Absolute RADiometer (DIARAD) and the Physikalisch-Meteorologisches Observatorium type 6 (PMO6) radiometers for the Variability of solar IRadiance and Gravity Oscillations (VIRGO) on the Solar and Heliospheric Observatory (SOHO) were estimated. It was concluded that the 0.35% observed discrepancy was large given the estimated uncertainties. A clear path forward was seen in the form of laboratory comparisons, which have now been realized as the TSI Radiometer Facility (TRF) at the Laboratory for Atmospheric and Space Physics (LASP) [11]. Values realized at TRF are traceable to the NIST Primary Optical Watt Radiometer (POWR) cryogenic radiometer, which realizes optical power with an uncertainty of 0.02% ($k = 1$) [15]. The TRF results indicate that excess scattering from the forward, view-limiting aperture, a design typical of all the historical TSI instruments but TIM, can lead to an overestimate of TSI. Quantification of scatter using representative flight sensors in experimental measurements, along with direct laboratory comparisons and consistent modeling of diffraction effects has demonstrated the outstanding utility of these efforts for reconciliation of the historical TSI discrepancies [16].

E. Aperture Area

The subject of this work is the aperture area uncertainty. For this component to be small, e.g., a relative uncertainty in the area of less than 0.01%, the radius of a precise circular aperture that is 8 mm in diameter, for example, must have an uncertainty less than 0.2 μm. In addition, different methods of determining the effective optical area, if accurate, must be consistent with each other, and the aperture area must remain constant in time (e.g., no oxidation or distortion). The realistic assignment of the uncertainty in the prelaunch measurement of aperture area is difficult and is best assessed by a measurement comparison program. In a May 2000 calibration workshop for the TIM instrument on the Earth Observing System (EOS) SORCE mission, the participants endorsed the idea of holding a comparison program on aperture area measurement with NIST serving as the hub institution [17]. The comparison presented in this paper is in response to that endorsement. It is consistent with the goals of the EOS calibration/validation program [18,19] and complements the previous radiometric comparisons [20,21] and comparisons on bi-directional reflectance [22].

The goal of the aperture comparison is to quantify the relative differences in measurements of the aperture area made by or for institutions involved in the on-orbit measurement of TSI and those made by NIST. That is, we aim to put all aperture area measurements on a common scale and assess the aperture measurements and their stated uncertainties, if possible. The initial requirement for participation, outlined in the NASA/NIST protocols, was that the aperture could be linked to the historical TSI results and that the area had been determined at the time of preflight characterization using the same technique and measurement system that had been used for the flight apertures. The participants were requested to provide the apertures, the values of the areas and uncertainties in these values, and associated documentation. The TIM/SORCE team was excluded from the comparison because NIST provided the aperture area measurements for that program [14] and has continued to provide aperture area determinations for subsequent TIM missions (see Table 1). The relative expanded uncertainties ($k = 2$) for the SORCE/TIM aperture areas were estimated to be 0.005% [23]. The measurements began in May 2003 and were completed in January 2007. Preliminary results have been reported [24] and [13].

F. Aperture Fabrication

Precision apertures are fabricated by mechanical methods, electrodeposition, etching, and laser drilling. Mechanically produced apertures require skilled craftsmanship and high-quality, well-maintained machines. The conventional mechanical method utilizes a high-accuracy lathe that turns or grinds the material to the desired rough shape, which is then lapped to the desired size and final shape. The lapping and turning process often produces an unwanted burr at the edge [25]. An improvement on this process utilizes a diamond-turning machine to make the final cut(s). The diamond-turning process makes very sharp cuts and produce edges with minimal burrs. Soft or hard metals can be used to make apertures using these mechanical methods, although harder materials are preferred for the conventional lapped method because this produces sharper edges. Either mechanical method can produce "cylindrical" apertures, where a short vertical wall about 70 μm in height (thickness), called a land, is left for the purpose of allowing a contact probe to measure the diameter using this surface. However, only diamond turning can produce knife-edged apertures where the thickness of the land is of the order of a few tens of nanometers. The diamond-turning process produces superior edge quality and circularity, with the deviation from roundness [26] less than 0.1 μm, compared to the 1 to 2 μm possible with conventional turning [27]. Both types of turning methods require significant time to make the final edge, which makes either mechanical process an expensive process for producing apertures. Electrodeposition is used to make good quality small apertures. For electrodeposition, a photo mask of approximately the same size and shape as the desired aperture is photo-produced on a phosphor bronze substrate. Metals such as copper or nickel are electrodeposited until the metal layer is slightly thicker than the mask. The photoresist is then dissolved, and the aperture removed from the substrate. Etching is similar except that the photoresist image is produced on the material itself. The area not covered by the resist is then etched out, producing the aperture. Both of these processes produce apertures, which have a very thin land. The edges are generally without burrs, but they are also very thin and easily deformed. As such, they cannot be measured using a contact method, but they are inexpensive to produce in quantity and are commercially available.

G. Aperture Measurement Methods

Traditionally, diameter values at several points along the circular aperture are determined by translating a ball-ended stylus from one edge to the other with diameter-measuring machines. This method requires a land to define the point of contact; diamond-turned apertures with knife edges would be damaged using this approach. The surface of the land is a source of reflected and scattered light, thus increasing the uncertainty in the optical area. It is the optical area that must be known, and this includes the forward-scattered flux, where the amount of scattered light depends on the characteristics of the incoming radiation such as beam convergence and wavelength.

Noncontact measurement methods were introduced to make it possible to measure apertures with knife edges. The noncontact methods can be either the flux ratio method, where the ratio of radiant flux transmitted through an aperture of known area is compared to that through a test aperture [28,29], or a geometric area measurement method similar to the contact probe method except that edge detection is made optically [30].

2. Comparison Apertures

Four laboratories participated in this comparison. Each laboratory sent their apertures to NIST for measurement using the NIST noncontact method.

The apertures submitted for the comparison are described below along with heritage information.

A. Royal Meteorological Institute of Belgium DIARAD Apertures

The Royal Meteorological Institute of Belgium (RMIB) DIARAD instrument is a type of dual-active-cavity radiometer developed by the RMIB in the 1970s [31,32]. Originally given the name CROM [33,34] and renamed in the mid-1990s, the basic DIARAD design has flown on a series of space missions with progressive improvements to the basic instrument design, particularly in the determination of the electrical heating of the cavity. Individual radiometers of the DIARAD type known as the DIARAD/SOLar CONstant experiment (SOLCON) have flown on short-term validation missions using the space shuttle [35]. SOLCON I was on board Spacelab 1 [36,37] SOLCON II was on board the Atmospheric Laboratory for Applications and Science 1 (ATLAS-1) [38], ATLAS-2 [39], ATLAS-3 [40], and the Hitchhiker/International Extreme ultraviolet Hitchhiker-03 (IEH-03) mission [35]. A version of SOLCON II, the SOlar constant and VAriability 1 (SOVA-1) flew on the Hitchhiker/Technology Applications and Science-01 (TAS-01) [35]. SOLCON III was part of the Hitchhiker/Fast Reaction Experiments Enabling Science and Technology Applications and Research (FREESTAR) mission that was lost on Shuttle Flight 107 in February 2003. The EUropean REtrievable CArrier (EURECA) mission was deployed and retrieved using different space shuttle flights; a SOVA-1 was flown as part of the SOlar VAriability experiment (SOVA) experiment [41,42]. In addition to these shuttle-borne flights, a DIARAD radiometer was operated as part of the SOlar Variable and Irradiance Monitor (SOVIM) instrument package on the International Space Station (ISS) [43,44]. Since 1995, a DIARAD radiometer has been operating in the VIRGO instrument package [45] on board the SOHO satellite. Finally, there is a DIARAD instrument as part of the SOlar VAriability PICARD (SOVAP) package [46,47] on board the PICARD satellite [48,49] that was launched in June 2010.

We refer to the group of shuttle-borne measurements using the SOLCONs, as DIARAD/SOLCON; the shuttle-deployed and retrieved SOVA-1 in SOVA on EURECA as DIARAD/SOVA; the SOHO-borne VIRGO experiment as DIARAD/VIRGO; the ISS-borne experiment as DIARAD/SOVIM; and the PICARD-borne DIARAD in SOVAP as DIARAD/SOVAP. The nominal diameters of the flux-limiting apertures, d, were 8 mm for early missions and increased to 10 mm for later missions. Figure 2 shows a simplified drawing of the DIARAD/VIRGO heritage aperture adapted from [50]. The dimensions are $d = 8$ mm (nominal), 28 mm outside diameter, thickness of 4 mm, and a land of 0.1 mm. The side facing the sun is concave spherical in shape, with a radius of curvature of 282 mm. The bevel on the detector side is also concave spherical in shape, with a radius of curvature of approximately 60 mm.

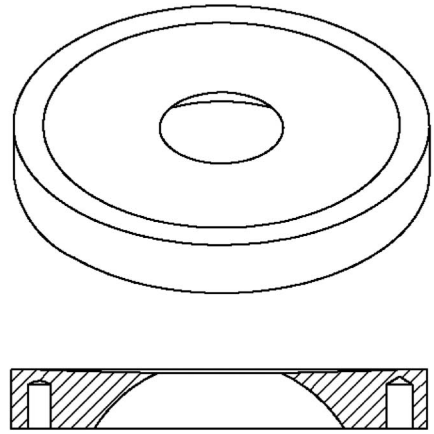

Fig. 2. Schematic of a DIARAD/VIRGO aperture with 8 mm inner diameter, 28 mm outer diameter, thickness of 4 mm, spherical front surface, spherical bevel, and 0.1 mm land. The RMIB comparison apertures with the exception of #5 and #8.5 were similar in design, but with different nominal inner and outer diameters and overall thicknesses.

A total of 12 apertures were submitted by RMIB for the comparison. The six apertures designated 1S to 6S by RMIB have $d = 10$ mm (nominal), 28 mm outside diameter, thickness of 5 mm, and a land of 0.1 mm (see Table 2). As with the DIARAD/VIRGO aperture illustrated in Fig. 2, the front surface and bevel are spherical in shape. Apertures 1S and 2S are titanium (with 6% aluminum and 4% vanadium) while 3S to 6S are stainless steel (with 19% to 20% chromium and 8% to 10.5% nickel). Apertures 1S and 2S, which are less reflective than 3S to 6S, are part of the DIARAD/PICARD program, apertures 3S and 5S are part of the DIARAD/SOVIM program, and apertures 4S and 6S are spares. For these six apertures, RMIB supplied values for d from two institutions: the NASA Jet Propulsion Laboratory (JPL), USA, and the National Physical Laboratory (NPL), UK. The NPL values were used for flight; they measured the diameters of 1S, 2S, 3S, and 5S for RMIB using a ball-ended stylus at four locations equally spaced around the circumference. The results were corrected to 20°C by NPL, and the expanded uncertainties ($k = 2$) are given in the last row in Table 3. The average of the four diameters was used to calculate the RMIB area, A_{RMIB} (see Table 9). NIST measured the 4S and 6S apertures, but since no RMIB/NPL values were available, these results are not included in the comparison, leaving 10 apertures in total (see Table 2).

The four apertures with the RMIB designations #3, #8, #9, and #10 are similar in design to the 1S to 6S series in that they are made of stainless steel (Type AISI 420), the front surface is spherical with a radius of curvature of 282 mm, the bevel is also spherical, and $d = 10$ mm (nominal). All four are part of the SOLCON and SOVA-1 (EURECA) aperture series; apertures #3 and #9 flew on EURECA.

Table 2. Apertures Submitted by the Institutions, with the Comparison Designation, the Institution and its Designation, the Material, Nominal Value of d, and the Source and Date of the Submitted Aperture Values and Uncertainties

Comparison Aperture	Institution	Institution Name	Material	Nominal d (mm)	Data Source
1	RMIB	1S	Ti	10	NPL (2000)
2	RMIB	2S	Ti	10	NPL (2000)
3	RMIB	3S	SST	10	NPL (2000)
4	RMIB	5S	SST	10	NPL (2000)
5	RMIB	#10	SST	10	SMD (1984)
6	RMIB	#8	SST	10	SMD (1984)
7	RMIB	#5	SST	5	NPL (1985)
8	RMIB	#8.5	SST	8.5	NPL (1985)
9	RMIB	#3	SST	10	SMD (1984)
10	RMIB	#9	SST	10	SMD (1984)
11	PMOD/WRC	PMO609	SST	5	METAS (1984)
12	PMOD/WRC	PMO611	SST	5	METAS (1984)
13	PMOD/WRC	SOVA R 111	SST	5	METAS (1988)
14	PMOD/WRC	SOVA R 113	SST	5	METAS (1988)
15	PMOD/WRC	VIRGO 2	SST	5	METAS (1992)
16	PMOD/WRC	VIRGO 3	SST	5	METAS (1992)
17	LaRC	A	Al	8	TRW (1985)
18	LaRC	C	Al	8	TRW (1985)
19	LaRC	D	Al	8	TRW (1985)
20	LaRC	307NS	Cu	6.3	TRW (1985)
21	JPL	ACRII 1	Al	8	JPL (2006)
22	JPL	ACRII 2	Al	8	JPL (2006)
23	JPL	ACRIII 1	Al	8	JPL (2006)
24	JPL	ACRIII 2	Al	8	JPL (2006)
25	JPL	ACRIII 3	Al	8	JPL (2006)

For this comparison, RMIB supplied values for d from two institutions: the Ministére des affaires économiques, service de métrologie (SMD), Belgium and the Test Service Division at the European Space Agency, European Space Research Technology Centre (ESA-ESTEC), Netherlands. Different methods were used, with determination of four diameters equally spaced around the circumference. The SMD results, which utilized noncontact optical microscopy with laser interferometry at 20°C, were used for flight values. The last row of Tables 3 and 4 give the SMD expanded uncertainty $u(d)$ for these apertures, and in Table 9 the area determined from the mean diameter.

The remaining two apertures, RMIB designations #5 and #8.5, differ in design in that the front surface and bevel are angled. Made of stainless steel (Type AISI 420), #5 has $d = 5$ mm (nominal) and an outer diameter of 20 mm; #8.5 has $d = 8.5$ mm (nominal) and an outer diameter of 40 mm. Both have a thickness of 2 mm and finite land. A dot on the surface of the aperture marks the reference direction and is the side that normally faces the sun. These apertures are from the DIARAD/SOLCON and DIARAD/SOVA programs and were measured in an international comparison activity from 1982 to 1986, with seven laboratories making measurements: SDM, ESA-ESTEC, NPL, NIST, the FDO, Netherlands, Bundesamt für Messewesen Lindeweg, Switzerland, and the National Physical Research Laboratory, South Africa. RMIB used the NPL results for flight instruments, which were taken at two locations, spaced 90° apart, and reported at 20°C. The coverage factor for the reported uncertainty value of 0.5 μm was not stated, but NPL reported that there were unassigned uncertainty

Table 3. Uncertainty Components for the RMIB Apertures[a]

Inst.	Unc.	1S	2S	3S	5S	#10
NIST	$u_{\mathrm{fit}}(r)$	53.1 nm	55.9 nm	17.6 nm	26.9 nm	335.1 nm
NIST	$u_{\mathrm{stage}}(r)$	26.0 nm	26.0 nm	26.1 nm	26.1 nm	26.0 nm
NIST	$u_{\mathrm{image}}(r)$	4.0 nm	4.0 nm	4.0 nm	4.0 nm	4.0 nm
NIST	$u_{\mathrm{temp}}(r)$	4.3 nm	4.3 nm	8.7 nm	26.1 nm	5.0 nm
NIST	$u_{\mathrm{geom}}(r)$	41.0 nm	70.5 nm	43.8 nm	81.1 nm	4.1 nm
NIST	$u(r)$, $k = 1$	72.2 nm	93.9 nm	54.8 nm	93.2 nm	336.2 nm
NIST	$u(d)$, $k = 2$	0.289 μm	0.376 μm	0.219 μm	0.373 μm	1.35 μm
RMIB	$u(d)$, $k = 2$	0.5 μm	0.6 μm	0.96 μm	1.09 μm	1.0 μm

[a]The NIST uncertainty components are given for $k = 1$, along with the combined standard uncertainty in mean radius and the expanded uncertainty in diameter at $k = 2$ for the RMIB apertures 1S, 2S, 3S, 5S, and #10. The expanded uncertainties at $k = 2$ in the measured aperture diameters for the previous measurements for the RMIB apertures are also given.

Table 4. Uncertainty Components for the RMIB Apertures[a]

Inst.	Unc.	#8	#5	#8.5	#3	#9
NIST	$u_{\text{fit}}(r)$	16.1 nm	21.3 nm	30.0 nm	77.1 nm	95.4 nm
NIST	$u_{\text{stage}}(r)$	26.0 nm	13.0 nm	22.1 nm	26.0 nm	26.0 nm
NIST	$u_{\text{image}}(r)$	4.0 nm	4.0 nm	4.0 nm	4.0 nm	4.0 nm
NIST	$u_{\text{temp}}(r)$	5.0 nm	2.5 nm	4.3 nm	5.0 nm	5.0 nm
NIST	$u_{\text{geom}}(r)$	2.6 nm	31.0 nm	4.3 nm	17.7 nm	34.5 nm
NIST	$u(r)$, $k = 1$	31.4 nm	40.1 nm	37.9 nm	83.5 nm	104.9 nm
NIST	$u(d)$, $k = 2$	0.125 μm	0.160 μm	0.152 μm	0.334 μm	0.420 μm
RMIB	$u(d)$, $k = 2$	1.0 μm	1.0 μm	1.0 μm	1.0 μm	1.0 μm

[a]The NIST uncertainty components are given for $k = 1$, along with the combined standard uncertainty in mean radius and the expanded uncertainty in diameter at $k = 2$ for the RMIB apertures #8, #5, #8.5, #3, and #9. The expanded uncertainties at $k = 2$ in the measured aperture diameters for the previous measurements for the RMIB apertures are also given.

components associated with the rounded shape of the land. We assumed the coverage factor for the stated uncertainties was $k = 1$, resulting in an expanded uncertainty in diameter to be 1.0 μm (see Table 4). The results of the NPL diameter determinations are in Table 9.

B. Physikalisch-Meteorologisches Observatorium Davos/World Radiation Center, PMO6 Apertures

The PMO6 [51] is a second-generation single-cavity activity radiometer developed by the Physikalisch-Meteorologisches Observatorium Davos, World Radiation Center (PMOD/WRC) in the 1970s. First-generation versions of the radiometer were used as part of the World Radiometric Reference (WRR) [52,53]. Over the succeeding decades, there have been incremental changes to the original PMO6 design [53], principally to the control and analog electronics. Initially, PMO6-type radiometers were flown on rocket and balloon packages [54,55]. Subsequently, PMO6 radiometers were flown as a pair on board EURECA as SOVA-2 in the SOVA experiment [56,57], with one instrument active and the other functioning as a backup. Currently, two PMO6 radiometers continue to make solar irradiance measurements as part of the VIRGO package on board SOHO [58–60]. In addition, PMO6 radiometers flew as part of the SOVIM package [43,61] on board the ISS. Finally, there are two PMO6 type radiometers in the PREcison MOnitoring Sensor (PREMOS) package [47] onboard PICARD [48,49]. As with the DIARAD radiometers, we refer to the PMO6 experiments as PMO6/SOVA for the EURECA payload, PMO6/VIRGO for the SOHO spacecraft, PMO6/SOVIM for the ISS payload, and PMO6/PREMOS for the PICARD spacecraft.

A total of six apertures were submitted by PMOD/WRC for the comparison (see Table 2). All have $d =$ 5 mm (nominal), a land of 0.02 mm, a bevel at 45°, and are made from lapped, hardened stainless steel (DIN × 46 Cr 13). The four apertures designated PMO609, PMO611, SOVA R 111, and SOVA R 113 (illustrated in Fig. 3) have outer diameters of 25 mm. The two designated VIRGO 2 and VIRGO 3 have outer diameters of 35 mm. All were measured in 1984 at the Federal Institute of Metrology (METAS), Switzerland, using a 3D touch probe at a depth of 0.01 mm at seven angles around the circumference. The stated uncertainty in the diameter for these measurements was 0.5 μm, with no coverage factor stated, and the roundness varied between 0.27 and 0.98 μm, depending upon the aperture. PMOD/WRC states the coverage factor for the METAS stated uncertainties was $k = 1$, resulting in an expanded uncertainty in diameter to be 1.0 μm (see the last row in Table 5). The METAS areas are given in Table 9.

Aperture PMO609 is part of the radiometer designated PMO609, which was originally fitted with a copper aperture [51]. For experiments in 1984 and later, the radiometer was fitted with aperture PMO609. The radiometer was flown as part of a set of rocket flights in a comparison with the active cavity radiometer irradiance monitor I (ACRIM I) on board the Solar Maximum Mission (SMM) [55], and in a series of Solar Irradiance Monitoring by BAlloons (SIMBA) balloon flights [62]. In addition, the instrument served as one of the intermediary radiometers in the 1990 comparison between the NPL Primary Standard Radiometer (PSR) [63] and the WRR [64]. Aperture PMO611 is mounted in the radiometer of the same designation. As with radiometer

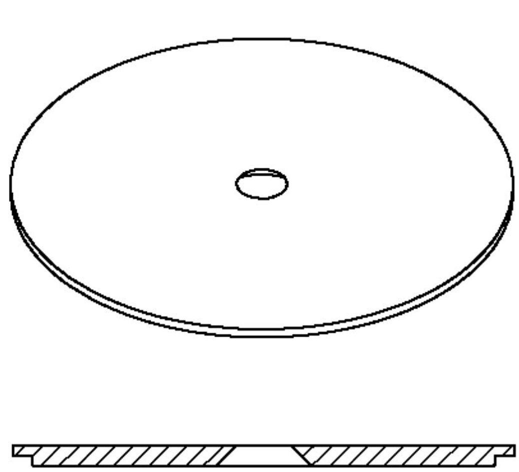

Fig. 3. Schematic of PMOD/WRC apertures PMO609, PMO611, SOVA R 111, and SOVA R 113. The nominal inner diameter is 5 mm, the outer diameter is 25 mm, the thickness is 2 mm, the land is 0.02 mm, and the bevel is at 45°.

Table 5. Uncertainty Components for the PMOD/WRC Apertures[a]

Inst.	Unc.	PMOD609	PMOD611	SOVA R 111	SOVA R 113	VIRGO 2	VIRGO 3
NIST	$u_{\text{fit}}(r)$	103.9 nm	41.7 nm	54.7 nm	17.4 nm	42.8 nm	20.7 nm
NIST	$u_{\text{stage}}(r)$	13.0 nm	13.0 nm	13.0 nm	13.0 nm	13.0 nm	13.0 nm
NIST	$u_{\text{image}}(r)$	4.0 nm	4.0 nm	4.0 nm	4.0 nm	4.0 nm	4.0 nm
NIST	$u_{\text{temp}}(r)$	7.9 nm	5.3 nm	5.3 nm	15.9 nm	2.6 nm	2.7 nm
NIST	$u_{\text{geom}}(r)$	60.4 nm	17.4 nm	9.3 nm	4.7 nm	5.6 nm	3.3 nm
NIST	$u(r)$, $k = 1$	121.3 nm	47.5 nm	57.4 nm	27.6 nm	45.3 nm	25.2 nm
NIST	$u(d)$, $k = 2$	0.485 μm	0.190 μm	0.230 μm	0.110 μm	0.181 μm	0.101 μm
PMOD/WRC	$u(d)$, $k = 2$	1.0 μm	1.0 μm	1.0 μm	1.0 μm	1.0 μm	1.0 μm

[a]The NIST uncertainty components are given for $k = 1$, along with the combined standard uncertainty in mean radius and the expanded uncertainty in diameter at $k = 2$ for the PMOD/WRC apertures. The expanded uncertainties at $k = 2$ in the measured aperture diameters for the previous measurements for the PMOD/WRC apertures are also given.

PMO609, radiometer PMO611 was flown on rockets in support of ACRIM I [55] and in the SIMBA balloon flights [62]. Radiometer PMO611 also served as one of the intermediary radiometers in a second comparison between the NPL PSR and the WRR [65] in 1994. Both PMO609 and PMO611 were part of the third international comparison between the WRR and the SI [66]. In addition, aperture PMO611 was part of a comparison of the geometric diameters of apertures from the NPL and the PMOD/WRC [27].

Apertures SOVA R 111 and SOVA R 113 were both flown in PMO6/SOVA on board EURECA [56,57]. In addition, the SOVA-R-111 apertures flew on ISS as part of the PMO6/SOVIM instrument [61]. The apertures VIRGO 2 and VIRGO 3 are from the two radiometers of the VIRGO flight instrument spare. Aperture VIRGO 2 was used on the SIMBA balloon flights [62], and aperture VIRGO 3 was part of the NPL and PMOD/WRC aperture comparison [27]. The VIRGO 2 radiometer participated in the comparison at the TRF facility in Boulder [16].

C. NASA Langley Research Center Earth Radiation Budget Experiment Apertures

The Nimbus 7 Earth Radiation Budget (ERB) instrument [67,68] was launched on board the Nimbus 7 satellite in October 1978. The instrument is a modified version of its predecessor on Nimbus 6, which did not contain an active cavity radiometer as one of its channels [69]. For the Nimbus 6 ERB, all of the solar channels measured portions of the spectrum, with channel 10S measuring the wavelength region from 0.243 to 0.312 μm [69]. For the Nimbus 7 ERB, that channel was modified to a Hickey–Frieden type (H-F type) cavity radiometer and renamed channel 10C (see Fig. 1 of [70]). That channel, the solar monitor on the Nimbus 7 ERB, has also been called H-F in the literature [71–73].

The ERBE was developed at the NASA Langley Research Center (LaRC) [74,75] and was flown on the ERBS and the National Oceanic and Atmospheric Administration (NOAA) NOAA 9 and NOAA 10 satellites in 1984, 1985, and 1986, respectively. For these satellites, each ERBE had a scanning and a nonscanning unit, with each nonscanning unit containing a solar monitor. The three ERBEs were essentially identical instruments [76], with flight unit 1 flown on ERBS (1984–2005), flight unit 2 on NOAA 9 (1985–1989), and the proto-flight unit on NOAA 10 (1986–1987). The ERBE solar monitors are direct descendants of the ACRIM I cavity radiometer on SMM [75,77]. None of the apertures from the Nimbus 7 program were available for this comparison.

A total of four apertures were submitted by NASA LaRC for comparison (see Table 2). Apertures A, C, and D are from a set of seven aluminum apertures made for the ERBE missions, and they played a role in ground support equipment or served as flight spares; another three of the seven were installed in ERBS, NOAA 9, and NOAA 10. All have $d = 8$ mm (nominal), an outer diameter of 48.5 mm, a thickness of 8.1 mm, and a bevel at 45° (see Fig. 4). Aperture 307NS is associated with a ground reference instrument and has $d = 6.3$ mm (nominal); it differs in design from the ERBE apertures in that the aperture is integrated into a cylindrical tube, with stepped internal diameters and a mounting flange at the base. The thickness of the land was not specified for any of the apertures. These four apertures were measured at Thompson Ramo Wooldridge, Inc. (TRW) in April 1985 utilizing a 0.635 cm diameter touch probe in an automated fashion for determination of the diameters at 16 locations around the circumference. In the LaRC 1985 internal report, the uncertainty of each radius measurement at TRW was estimated to be 2.54 μm, but no information was given on the combined uncertainty in the mean radius. We adopt this value as a $k = 1$ uncertainty in

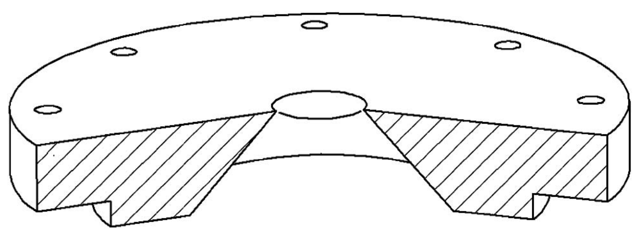

Fig. 4. Schematic of the LaRC aperture type A, C, and D used for ERBE. The nominal inner diameter is 8 mm, the outer diameter is 48.5 mm, the thickness is 8.1 mm, and the land, which exists, was not specified. The bevel is at 45°.

Table 6. Uncertainty Components for the LaRC Apertures[a]

Inst.	Unc.	A	C	D	307NS
NIST	$u_{\mathrm{fit}}(r)$	1.32 μm	1.81 μm	2.46 μm	0.967 μm
NIST	$u_{\mathrm{stage}}(r)$	20.9 nm	21.0 nm	21.0 nm	16.5 nm
NIST	$u_{\mathrm{image}}(r)$	4.0 nm	4.0 nm	4.0 nm	4.0 nm
NIST	$u_{\mathrm{temp}}(r)$	9.3 nm	9.4 nm	9.4 nm	5.3 nm
NIST	$u_{\mathrm{geom}}(r)$	33.8 nm	31.3 nm	31.4 nm	130.4 nm
NIST	$u(r)$, $k = 1$	1.32 μm	1.81 μm	2.46 μm	0.976 μm
NIST	$u(d)$, $k = 2$	5.29 μm	7.24 μm	9.84 μm	3.91 μm
LaRC	$u(d)$, $k = 2$	10.16 μm	10.16 μm	10.16 μm	10.16 μm

[a]The NIST uncertainty components are given for $k = 1$, along with the combined standard uncertainty in mean radius and the expanded uncertainty in diameter at $k = 2$ for the LaRC apertures. The expanded uncertainties at $k = 2$ in the measured aperture diameters for the previous measurements for the NASA LaRC apertures are also given.

the radius, giving an expanded uncertainty in the diameter of 10.16 μm ($k = 2$) (see the last row in Table 6). The LaRC areas are given in Table 9.

D. NASA JPL ACRIM Apertures

The spacecraft-borne ACRIM radiometers are part of a series of Active Cavity Radiometers (ACRs) developed at NASA JPL in the 1960s [78–80] for use in laboratory environmental simulators and for measurements of TSI. Measurements from two of the earlier ACR-type III radiometers are part of the definition of the WRR in 1975 [52]. The spacecraft-borne ACRs, ACR-type IV, were modified from the earlier versions by reducing the size of the aperture, inclusion of a reference cavity connected back-to-back with the solar cavity, use of specular (not diffuse) black paint, and other changes [81]. ACR-type IV radiometers were flown on a series of rocket flights from 1976 to 1986 [73]. In 1980, three ACR-type IV radiometers were launched as channels A, B, and C of the ACRIM I instrument package [82,83] on board the SMM satellite. The three were operated independently with different exposure times to determine the degradation in responsivity due to solar exposure [55]. In the late 1970s, the ACR-type V was developed, using a process to reduce the formation of a meniscus-enhanced cavity reflectance at the apex of the cavity during the application of the specular black paint [84]. Radiometers of this type were flown in instrument packages as part of the ATLAS-1, ATLAS-2, and Spacelab 1 missions on board the space shuttle [85]. A variant of the shuttle instrument package was flown as the ACRIM II instrument package [85] on-board the Upper Atmosphere Research Satellite (UARS), which was launched in 1991 and made measurements through 2001. The ACRIM III instrument package [86] was launched aboard ACRIMSAT in 1999 [87]. Each of the three radiometers in ACRIM III are ACR-type V; however, the total mass and volume of instrument package was reduced by more than a factor of two compared to the ACRIM II instrument package [86].

Five apertures from NASA JPL were sent to NIST for comparison (see Table 2). Apertures ACRII 1 and 2 and ACRIII 1, 2, and 3 are associated with the ACR-type V radiometers used in ACRIM II and ACRIM III, respectively. All have $d = 8$ mm (nominal), an outer diameter at the aperture of 24.08 mm, and a bevel at 41° (see Fig. 5). The ACRIM apertures were designed using heat retention and conduction considerations, since they are part of the cavity of the instrument, with a total length of 47 mm and an outer diameter of 42.04 mm. The overall dimensions required modifications to the NIST aperture measurement system. The modifications and validation procedures are described in [88]. None of the apertures had final polishing, and none were fully representative of (as good as) the actual flight apertures. The diameters of the apertures were measured in the JPL metrology laboratory in January 2006, using an optical comparator. The ACRIM flight apertures were not measured using this machine, and a comparison between the current and previous machines at JPL is not available. The expanded uncertainties, given at $k = 2$ in the last row of Table 7, were calculated from the uncertainty in the mean of the six measurements. The NASA JPL values for the aperture areas and relative uncertainties $u(A)/A$ are given in Table 9.

3. NIST Measurement Method and Uncertainties

The method adopted at NIST for measurement of aperture areas is a noncontact method, employing an interferometrically controlled XY stage that

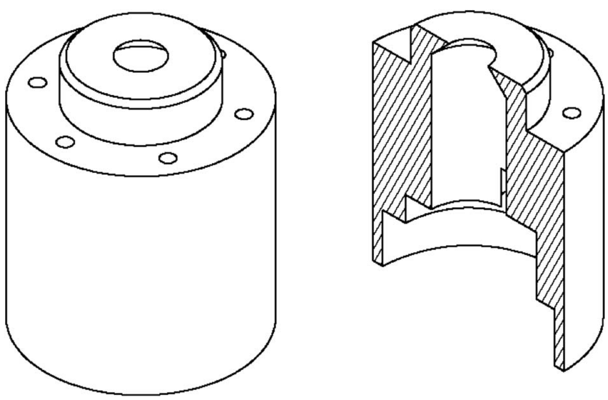

Fig. 5. Schematic of the ACR type apertures used for ACRIM. The aperture is at the end of a baffle tube assembly that mounts to the cavity. The nominal inner diameter is 8 mm, the outer diameter at the aperture is 24.08 mm, the total length is 47 mm, and the bevel is at 41°.

Table 7. Uncertainty Components for the JPL Apertures[a]

Inst.	Unc.	ACRII 1	ACRII 2	ACRIII 1	ACRIII 2	ACRIII 3
NIST	$u_{\text{fit}}(r)$	168.5 nm	366.6 nm	179.3 nm	499.3 nm	197.0 nm
NIST	$u_{\text{stage}}(r)$	21.1 nm	20.8 nm	20.7 nm	20.9 nm	20.7 nm
NIST	$u_{\text{image}}(r)$	4.0 nm	4.0 nm	4.0 nm	4.0 nm	4.0 nm
NIST	$u_{\text{temp}}(r)$	9.4 nm	9.3 nm	9.2 nm	9.3 nm	9.2 nm
NIST	$u_{\text{geom}}(r)$	18.8 nm	21.4 nm	9.8 nm	5.8 nm	13.5 nm
NIST	$u(r)$, $k = 1$	171.2 nm	368.0 nm	181.0 nm	499.9 nm	198.8 nm
NIST	$u(d)$, $k = 2$	0.685 μm	1.47 μm	0.724 μm	2.00 μm	0.795 μm
JPL	$u(d)$, $k = 2$	3.24 μm	3.41 μm	3.48 μm	9.43 μm	1.26 μm

[a]The NIST uncertainty components are given for $k = 1$, along with the combined standard uncertainty in mean radius and the expanded uncertainty in diameter at $k = 2$ for the JPL apertures. The expanded uncertainties at $k = 2$ in the measured aperture diameters for the previous measurements for the NASA JPL apertures are also given.

translates the test sample under a microscope with a charge-coupled device (CCD) camera to locate the edge points [89,90]. The measurement system consists of a broadband light source illuminating the sample from below through a Köhler illuminator, an air-bearing-supported, open-frame, XY stage with a heterodyne laser interferometer feedback system for xy axis positioning, a z axis translation stage carrying a microscope with long working distance objectives, the digital CCD camera, and a control computer. Figure 6 shows photographs of the instrument. Complete characterization of the whole system and all its components was performed, including straightness of axis travel and perpendicularity of the axes, when the facility was set up or moved. Only microscope alignment is performed routinely. The absolute dimensional metrology scale comes from the wavelength accuracy of the laser interferometer used for the stage travel. The laser distance scale had a resolution of 4 nm for this study, while the stage motion had a resolution of 25 nm.

To perform the measurements, the apertures are mounted on a custom-made mounting ring that is designed to be centered on and in plane with the XY stage, and the nominal aperture diameter and angular separation of the measurements are input to the program. The stage is "homed," with the reference

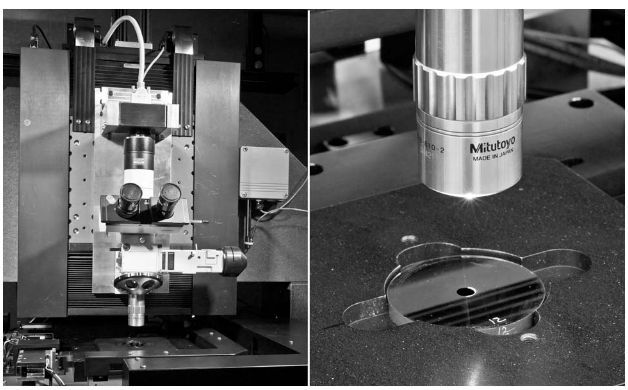

Fig. 6. Photographs of the NIST aperture measurement facility. Air bearings and a wavelength-compensated laser interferometer with nested XY stages move the aperture into the FOV of the CCD-based microscope that is mounted on the Z stage. The laboratory is optimized for thermal and vibrational stability.

location for the laser-based distance measurements established at the center of the XY stage. Then the stage moves along one coordinate until an aperture edge is detected, followed by movement in the opposite direction until the opposing aperture edge is detected. From a position halfway between, the stage repeats this procedure in the orthogonal direction. These four initial measurement points are used to establish the estimated aperture radius and center location using the circle-fitting algorithm.

Next, an automated focusing routine is used to determine the optimal focal plane for the aperture under study by adjusting the z axis translation stage. The method, which utilizes an automated Fibonacci search algorithm, is based on the fact that the modulation transfer function of an optical system is maximum at the optimum focal location. The optimum focus is determined in 45° increments around the circumference of the aperture. Optimum focal locations at other azimuthal angles are found by interpolation and are adjusted for each edge determination.

Following these initialization procedures, measurements are made for sequential edge locations, moving around the circumference in the desired steps. Using the estimated parameters for radius and aperture center with the stage reference location and the laser-based distance scale to determine the amount of stage motion, an edge is brought into view with motion in one axis. The field-of-view (FOV) of the CCD camera corresponded to an object diameter of about 0.2 mm at the aperture plane. To avoid spherical aberrations, only the central portion of the camera-microscope optical system was utilized. Therefore the aperture edge of the 5 to 10 mm diameter apertures measured here appeared to have a large radius of curvature in the image.

At this point, the edge is within the camera's FOV, and the grey levels of all pixels are read, searching for transitions. To minimize aberrations in the edge-detection algorithm, the stage is moved until the edge coincides with the central camera pixel. The central row or column of pixels is scanned, and the pixel containing the edge is determined using the edge thresholding procedure described below. The absolute position of the central camera pixel and its relationship, in pixel units, to the pixel containing the edge is known, so with knowledge of pixel size (9.875 μm × 8.0 μm) and system magnification, $M = 17.7$, the stage is commanded to move in the appropriate axis and direction. The choice of axis to move depends on the location of the edge pixel: x for pixels within ±45° of the x axis and y for pixels within ±45° of the y axis, with the origin at the central camera pixel. At each move, the pixel containing the edge is re-determined using the edge-thresholding procedure, and when the stage resolution of 25 nm is reached, the process stops and a final edge thresholding is performed. This process is repeated, traveling around the aperture circumference at the desired angular steps, using the initial estimates of the aperture center and diameter to move to the next targeted edge point.

The assignment of an edge location to a pixel is based on measured light levels on either side of the edge accounting for diffraction and partial coherence as well as a subpixel correction [90]. The edge is assigned to be at 26.65% of the illuminated level, as determined from coherence modeling of edge waveforms using commercial software. Because the pixels are large, the process of edge thresholding involves a subpixel correction, C to the total distance traveled by the stage given by

$$C_x = \frac{pL_x \cos\beta}{M} \quad \text{and} \quad C_y = \frac{pL_y \sin\beta}{M}. \qquad (1)$$

Here L_x and L_y are the pixel lengths, β is the angular misalignment of the XY stage to the camera's CCD pixels, and p, determined by linear interpolation in the row (or column) of pixels, is the fractional pixel length required to achieve the desired relative 26.65% light level given the actual measured relative light level. Thus the edge coordinate location, (x_i, y_i), in the stage reference frame depends on counting fringes [stage location (X_s, Y_s)] as well as the camera metrology, system focus, stage-camera alignment, coherence modeling, and estimates of p (subpixel correction C):

$$x_i = X_S \pm C_x \quad \text{and} \quad y_i = Y_S \pm C_y. \qquad (2)$$

For the majority of the RMIB apertures and all of the PMOD/WRC apertures, measurements were made in increments of 1° around the circumference, resulting in 360 (x_i, y_i) pairs of values. For RMIB 2S, #3, and #9 and all of the LaRC and JPL apertures, the increment was 5°; for RMIB 1S, the increment was 10°. Multiple runs were taken, with the aperture removed, rotated, and replaced between each measurement set. For the majority of the RMIB and all of the PMOD/WRC apertures, six sets were taken, and the rotation was 59.3° between each set. For the LaRC and JPL apertures, five sets were taken, and the rotation was 61.3°. For the JPL apertures, an additional set of five was acquired in January 2007. Each set was independently fit to a circle [91]. The resulting mean radius was corrected for thermal expansion using the average temperature in Celsius T_j during set j according to

Table 8. Values for the Coefficient of Linear Expansion Used to Correct the NIST Measurement Results to 20°C[a]

Comparison Designation	Participant Designation	Material	α °C^{-1}
1, 2	1S, 2S	Ti	8.6×10^{-6}
3, 4	3S, 5S	SST	17.3×10^{-6}
5 to 10	#10, #8, #5, #8.5, #3, #9	SST	10.0×10^{-6}
11 to 16	PMO609, PMO611, SOVA R 111, SOVA R 113, VIRGO 2, VIRGO 3	SST	10.6×10^{-6}
17, 18, 19	A, C, D	Al	23.2×10^{-6}
20	307NS	Cu	16.7×10^{-6}
21 to 25	ACRII 1, ACRII 2, ACRIII 1, ACRIII 2, ACRIII 3	Al	23.2×10^{-6}

[a]Values for the aluminum and copper material were not provided by the participants, so typical values from a material database were used.

$$r_j(20°\mathrm{C}) = [(20°\mathrm{C} - T_j)\alpha + 1]r(T_j), \qquad (3)$$

where α is the coefficient of linear expansion per degree Celsius for the aperture material. The values for α used in the correction and uncertainty analysis are given in Table 8. The average value for the radius, $r(20°\mathrm{C})$, was determined from the six sets, and this was used to determine the aperture area. The data for each set were also fit to an ellipse for the purpose of comparison [92].

The estimates for the NIST uncertainties in the mean radii for the participants' apertures are given in Tables 3 and 4 for RMIB, Table 5 for PMOD/WRC, Table 6 for LaRC, and Table 7 for JPL. There are five components to the uncertainty. The combined uncertainty in the radius is the root sum of squares of the five components. The first, $u_{\mathrm{fit}}(r)$, is a Type A uncertainty [93] associated with the circle-fitting procedure. The sources of this uncertainty are the random component of the stage position as well as imperfections in the aperture edge. The bootstrap method was utilized [94] on each set of measurements. This is a Monte Carlo-based resampling of the original data set followed by a new determination of the mean radius and center coordinates. The variance in the mean radius was determined from 5000 such runs for each of the sets, and the average was used to estimate the standard uncertainty, $u_{\mathrm{fit}}(r)$, in mean radius.

The interferometer-based stage positioning has a systematic uncertainty that is proportional to the travel distance. A Type B scaling factor of 2.6×10^{-6} nm/nm was estimated, and the uncertainty $u_{\mathrm{stage}}(r)$ determined using the aperture diameter for the travel distance: $u_{\mathrm{stage}}(r) = 2.6 \times 10^{-6}\, d$ at $k = 1$. The Type B uncertainty in the subpixel correction, $u_{\mathrm{image}}(r)$, was determined by propagating uncertainties using the measurement equation, Eq. (1), and evaluating the uncertainties in the contributing parameters (p, L, β, and M) via experimental testing; this gave $u_{\text{image}}(r) = 4$ nm ($k = 1$). There is a random component to the imaging due to source and detector fluctuations, but this contributes negligible uncertainty to the mean radius.

The ambient temperature was measured before and after each run, and the average temperature was used to correct the areas to 20°C. The maximum temperature differences were used to estimate the temperature uncertainty, and from propagation of the measurement equation [Eq. 3)], the corresponding uncertainty in radius is $u_{\text{temp}}(r) = r\,\alpha\,u(T)$ at $k = 1$. The temperature variation during a measurement was typically 0.1°C and at most 0.6°C. The final Type B uncertainty is related to geometry, specifically the mounting of the aperture. Any tilt of angle θ between the aperture plane normal and the stage axis z will result in scaling of the measured area by the factor cos θ. The tilt angle was estimated from the average of the maximum differences in optimum focus positions for each set, giving $u_{\text{geom}}(r) = r(1 - \cos\theta)/2$ at $k = 1$. The average angular tilt was 0.28° over all comparison apertures. No correction for this effect was performed. It should be noted that this uncertainty estimation does not take into account the warped sections, if any, of the aperture.

The NIST Sensor Science Division aperture measurement facility has been validated by participation in international comparisons. The facility was the pilot laboratory for the international comparison on aperture area measurements for radiometry, termed S2, conducted by the Consultative Committee on Photometry and Radiometry (CCPR), which spanned from 1999 to 2003 [95]. No significant measurement drift was detected over that interval of time using several dedicated control apertures. Similarly, using the control apertures, no drift was detected over the course of this comparison. As in this comparison, the CCPR S2 comparison included apertures with lands, which were measured using contact and noncontact methods. The measured areas by the contact method generally registered higher than the noncontact method, although well within the stated uncertainties of both methods, which render the differences insignificant.

4. Results of the Comparison

In Tables 3 and 4 (RMIB), 5 (PMOD/WRC), 6 (LaRC), and 7 (JPL), the individual components are stated in terms of the uncertainty in the measured radius as well as the combined standard uncertainty in radius and the combined expanded uncertainty in diameter. The term $u_{\text{image}}(r)$ is negligible in all cases, and the term $u_{\text{temp}}(r)$ is not generally significant in relation to the other components. In general, the overall uncertainty is dominated by $u_{\text{fit}}(r)$, with $u_{\text{geom}}(r)$ and $u_{\text{stage}}(r)$ being strong contributors; this indicates that, for these apertures, the uncertainty is determined primarily by the quality of the edge, the flatness, and/or mechanical mounting of the aperture, and the systematic component of the stage movement. Comparison of the NIST uncertainties to those provided by the participants indicates that in some cases they are equivalent, but for the most part the NIST uncertainties are smaller in magnitude.

None of the participants supplied detailed uncertainty budgets that would meet the guidelines outlined in international standards documents such as the *Guide to the Expression of Uncertainty in Measurement* (GUM) [96]. Adherence to the GUM would include stating the source of the components, whether they were Type A or Type B, and giving the coverage factor k. The documentation supplied was variable in terms of detail, with some being quite sparse. Incorporation of the values required use of scientific judgment in some instances. Examples include the apparent reversal of labeling of tables for RMIB 1S, 2S, 3S, and 5S; discrepancies between the laboratory documentation provided by the measuring laboratory and the documentation provided by the participant to NIST and multiple statements on the uncertainty values. Some participants indicated they included the roundness measure in the uncertainty estimate [32, 97] while others separately specified $u(d)$ and the roundness value. We did not include any separately stated roundness values in the participant's uncertainty estimates, e.g., for PMOD/WRC. There were instances where factors that had an impact on the measured diameters were identified but not corrected for, such as the shape of the land (making it difficult to establish the plane of the aperture), drift between subsequent measurements, perpendicularity to the aperture plane, and operator factors in visual-based systems. The LaRC documentation for apertures A, C, and D states the individual eight or nine values used to determine the mean radius. Because the uncertainty in the mean is comparable to the stated uncertainty, we suspect the LaRC reported uncertainty is only the Type A component, from the standard deviation for replicate measurements. For JPL, this was the only component supplied, and we note that the value is consistent with the relative area uncertainty reported at the TSI workshop [13].

The results of the measurement comparisons for each participating laboratory are summarized in Table 9 and Fig. 7. In Table 9, the fourth and fifth columns state the areas of the apertures using the NIST instrument and the NIST relative expanded uncertainty in the area. The sixth and seventh columns show the areas of the apertures and their relative expanded uncertainty as obtained from the participant-supplied measurements results. The eighth column is the ratio of the participant area to the NIST area. The ninth column is the relative expanded uncertainty in these ratios.

In Fig. 7, the RMIB and PMOD/WRC ratios are plotted as a function of the comparison aperture identification (1 through 16) using the left-hand ordinate. The $k = 2$ uncertainties in the ratios are

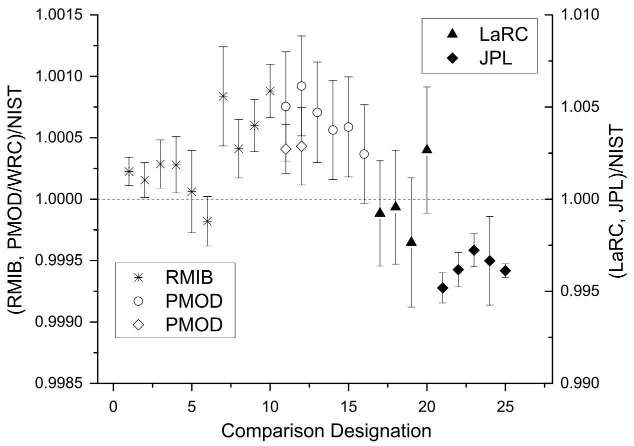

Fig. 7. Results of the aperture area comparison shown as the ratio of the participant area normalized by the NIST area. The vertical lines are the $k = 2$ uncertainty in these ratios. RMIB and PMOD/WRC are plotted using the left ordinate; LaRC and JPL are plotted using the right ordinate.

shown as vertical lines. For these RMIB and PMOD/WRC apertures, the participant areas agreed with the NIST areas to within +0.09%, −0.02%. However, only two of the 16 ratios agree within the combined expanded uncertainties. The majority of the ratios are greater than unity, indicating either the RMIB and PMOD/WRC areas were overestimated or NIST's areas were underestimated.

Of the 10 RMIB apertures, six were measured by NPL in two groups, and four (RMIB numbers #3, #8, #9, and #10) were measured together in 1984 by SMD (see Table 2). Eight apertures were measured at NIST in 2002 and the remaining two (RMIB numbers #3 and #9) in 2005. The average ratio results for #8 and #10 are 0.08% less than the average ratio results for #3 and #9, and this is outside either laboratory's expanded uncertainties (see Table 9). It is noted that these four apertures are the only ones that are not internally consistent within the expected uncertainties. Measurements of the NIST control aperture during this interval varied less than 0.005%.

Two of the six PMOD/WRC apertures were remeasured by METAS in 2006 using a new facility for length and area measurements; this study also included detailed mapping of the shape of the land [98]. The 2006 results for the PMO609 and PMO611 areas were 0.03% and 0.05% lower than the 1984 results. The two METAS measurements agreed within their combined uncertainties at $k = 2$, but the 2006 results, although closer in agreement with NIST, still do not agree with NIST within the combined expanded uncertainty.

Also in Fig. 7, the LaRC and JPL ratios are plotted as a function of comparison aperture identification (17 through 25) using the right-hand ordinate, which differs in scale by almost an order of magnitude from the left-hand ordinate. The LaRC apertures agreed to within +0.235%, 0.267% and are within the comparison expanded uncertainties. The JPL apertures, like most of the RMIB and PMOD/WRC, do not agree with NIST within the expanded uncertainties, and

Table 9. NIST Measurement Results of Apertures and the Results Submitted by the Institutions[a]

Comp. Ap.	Inst.	Inst. Name	A_{NIST} (mm^2)	NIST $u(A)/A$	A_{Inst} (mm^2)	Inst. $u(A)/A$	A_{Inst}/A_{NIST}	$u(A_{Inst}/A_{NIST})$
1	RMIB	1S	78.7368	5.77E − 05	78.7545	9.99E − 05	1.00023	1.15E − 04
2	RMIB	2S	78.7534	7.50E − 05	78.7657	1.20E − 04	1.00016	1.41E − 04
3	RMIB	3S	79.3966	4.36E − 05	79.4193	1.91E − 04	1.00029	1.96E − 04
4	RMIB	5S	79.4422	7.41E − 05	79.4644	2.17E − 04	1.00028	2.29E − 04
5	RMIB	#10	78.4918	2.69E − 04	78.4966	2.00E − 04	1.00006	3.35E − 04
6	RMIB	#8	78.5037	2.51E − 05	78.4896	2.00E − 04	0.99982	2.02E − 04
7	RMIB	#5	19.7845	6.39E − 05	19.8010	3.98E − 04	1.00084	4.03E − 04
8	RMIB	#8.5	56.7972	3.57E − 05	56.8205	2.35E − 04	1.00041	2.38E − 04
9	RMIB	#3	78.3264	6.69E − 05	78.3734	2.00E − 04	1.00060	2.11E − 04
10	RMIB	#9	78.3605	8.40E − 05	78.4295	2.00E − 04	1.00088	2.17E − 04
11	PMOD/WRC	PMO609	19.5762	1.94E − 04	19.5910	4.00E − 04	1.00075	4.45E − 04
12	PMOD/WRC	PMO611	19.6546	7.59E − 05	19.6727	4.00E − 04	1.00092	4.07E − 04
13	PMOD/WRC	SOVA R 111	19.7030	9.17E − 05	19.7169	3.99E − 04	1.00071	4.10E − 04
14	PMOD/WRC	SOVA R 113	19.5808	4.42E − 05	19.5919	4.00E − 04	1.00056	4.03E − 04
15	PMOD/WRC	VIRGO 2	19.5771	7.26E − 05	19.5886	4.00E − 04	1.00059	4.07E − 04
16	PMOD/WRC	VIRGO 3	19.7567	4.02E − 05	19.7640	3.99E − 04	1.00037	4.01E − 04
17	LaRC	A	50.6085	1.32E − 03	50.5693	2.53E − 03	0.99923	2.85E − 03
18	LaRC	C	51.3070	1.79E − 03	51.2846	2.51E − 03	0.99956	3.09E − 03
19	LaRC	D	51.2521	2.44E − 03	51.1316	2.52E − 03	0.99765	3.50E − 03
20	LaRC	307NS	31.6356	1.23E − 03	31.7199	3.20E − 03	1.00267	3.43E − 03
21	JPL	ACRII 1	51.9351	1.68E − 04	51.6849	7.99E − 04	0.99518	8.17E − 04
22	JPL	ACRII 2	50.4882	3.67E − 04	50.2948	8.53E − 04	0.99617	9.29E − 04
23	JPL	ACRIII 1	49.8669	1.82E − 04	49.7287	8.75E − 04	0.99723	8.93E − 04
24	JPL	ACRIII 2	50.5308	4.99E − 04	50.3619	2.36E − 03	0.99666	2.41E − 03
25	JPL	ACRIII 3	49.8577	2.00E − 04	49.6641	3.18E − 04	0.99612	3.76E − 04

[a]The expanded relative uncertainties in area, $u(A)/A$, and the expanded uncertainties in the ratio A_{Inst}/A_{NIST}, are given at $k = 2$. The mean and standard deviation of the ratios by institution are RMIB, 1.00036 and 0.00034; PMOD/WRC, 1.00065 and 0.00020; LaRC, 0.99978 and 0.00021; and JPL, 0.99627 and 0.00076.

all of the ratios are less than unity by −0.281% to −0.486%, indicating JPL areas were underestimated or the NIST areas overestimated. It was not apparent that the LaRC or JPL areas were corrected for laboratory temperature, but this is a negligible correction given the magnitude of the observed differences, about ±0.02% for a ±5°C temperature difference.

5. Discussion

In spite of the general lack of agreement within the combined expanded uncertainties, the authors find the results to be satisfactory and that errors in flight aperture area determinations are not likely to be the source of the discrepancy in the historical TSI record. Note that if the aperture area for a flight instrument were underestimated, the derived TSI would be overestimated. The majority of our results indicate the opposite behavior, with participant areas greater than the NIST values. If aperture area was the main source to the discrepancy in flight TSI values, Fig. 7 should have a similar pattern, but inverted with respect to TIM, in Fig. 1 in [13], and this is not the case. This conclusion is independent of the NIST scale, since the TIM apertures were measured using the same NIST facility.

In addition, the magnitude of the discrepancies for RMIB and PMOD/WRC is too small to explain the TSI differences; for LaRC there is no discrepancy; and for JPL the observed discrepancy cannot be tied reliably to ACRIM flight aperture areas because the edges were not fully lapped and polished, a different measurement system was used by JPL in 2006 than what was used for ACRIM flight apertures prior to the missions, and no results were submitted that would establish the relationship between these two systems, e.g., measurements of control apertures.

Reasonable explanations for lack of agreement within the combined expanded uncertainties include the likelihood that the participant's uncertainties were underestimated and that some of the apertures may have changed since the time of the participant's measurements. It is recommended that future efforts report uncertainties according to the GUM, perform intercomparisons at the time of flight build, maintain a quality system, and manufacture, maintain (in clean storage), and repeatedly measure independent comparison apertures as control samples.

Most of the participants used contact methods to measure their aperture diameters, the exceptions being RMIB #8, #10, #3, and #9 (comparison apertures 5, 6, 9, and 10) and the five JPL apertures. NIST used a noncontact method. It is interesting to note that for the RMIB and PMOD/WRC apertures, this comparison, as with CCPR-S2, resulted in slightly larger diameters for the contact method compared to the NIST noncontact method. However, this trend is not observed in the four LaRC apertures, and the JPL results disagree, even though both areas resulted from noncontact methods. Therefore, a general statement about the nonequivalence of the geometric area measured using contact methods and the optical area measured using NIST noncontact method as an explanation for the observed discrepancies is not reasonable from these results.

The apertures varied significantly in their design, which will have an impact on their use in TSI instruments. Apertures manufactured with a bevel at 45°, such as PMOD/WRC and LaRC, may introduce extraneous light into the cavity by retro-reflection of scattered or reflected light from surfaces other than the cavity itself. However, in these TSI instruments, the aperture is the limiting aperture, and it is at the cavity entrance, so this effect should be negligible. The land, present to some extent on all apertures except knife-edge, diamond-turned ones, is a source of extraneous flux as the surface parallel to the optical axis acts like a lens for the low-divergence solar rays. Finally, all of the apertures differed in material and surface finish, attributes that will have an impact on the performance on orbit. In short, to best assess on-orbit performance, system-level comparisons, and calibrations of flight or flight-type sensors must be performed in the laboratory where the full effects of diffraction, inter-reflections, and scattering can be quantified [16].

The results presented here differ from those presented at the TSI workshop [13] in several respects. We have now included apertures #3 and #9 of RMIB (comparison apertures 9 and 10), as well as the five JPL apertures (comparison apertures 21 to 25). A data-entry error for the RMIB area for aperture #5 (comparison aperture 7) was discovered and corrected, reducing the previously reported discrepancy from 1.0068 to 1.00084. This point was an unexplained outlier in Fig. 2 in [13]. The LaRC documentation gave three independent area measurements. At the TSI workshop, the average was presented. Here we use only the contact results. Finally, we have corrected for previous errors in the coefficients of thermal expansion and the associated corrections in aperture areas.

In conclusion, for the RMIB and PMOD/WRC results in Fig. 7, the comparisons support a general agreement at better than 0.1%, with most of the results outside the expanded uncertainty in the comparison ratio. The LaRC results are in agreement within the expanded uncertainties. Discrepancies exist between the NIST and JPL areas. For RMIB, PMOD/WRC, and LaRC, the magnitude and sign of the differences are at odds with reconciling past TSI results, e.g., Fig. 1 in [13], and for JPL the lack of linkage between the apertures measured in this comparison and actual flight apertures precludes assessment of ACRIM TSI results with regard to aperture area differences.

It is likely that some, and possibly all, of the participant's uncertainties were underestimated. Adherence to the GUM was not uniform. The NIST uncertainties indicate that the major factors in the total uncertainty were often not associated with the NIST method but rather "environmental" in nature—the quality of the edge, $u_{\mathrm{fit}}(r)$ and the flatness of the aperture and the ability to mount it in plane with the moving stages, $u_{\mathrm{geom}}(r)$. Reducing these components is feasible by the manufacture of knife-edge diamond-turned apertures. The significant NIST component was the systematic error in the stage position, $u_{\mathrm{stage}}(r)$, which scales with travel distance. This component has now been better quantified using a 100 mm square grid plate, with the updated expression of $u_{\mathrm{stage}}(r) = 3.0 \times 10^{-7}\, d + 9$ nm at $k = 1$. For best results with apertures of these sizes and materials, the temperature during a single set should vary less than 0.1°C.

Appendix A: Acronym List

ACR	Active Cavity Radiometer
ACRIM	Active Cavity Radiometer Irradiance Monitor
ACRIMSAT	ACRIM SATellite
AISI	American Iron and Steel Institute
ATLAS	Atmospheric Laboratory for Applications and Science mission (on space shuttle)
CCD	Charge-Coupled Device
CCPR	Consultative Committee on Photometry and Radiometry
CROM	not an acronym, an early name for DIARAD
DIARAD	DIfferential Absolute RADiometer
EOS	Earth Observing System
ERB	Earth Radiation Budget experiment (on Nimbus 6 and 7)
ERBE	Earth Radiation Budget Experiment (on the ERBS, NOAA-9, and NOAA-10 satellites)
ERBS	Earth Radiation Budget Satellite
ESA-ESTEC	European Space Agency, European Space Research and Technology Centre
EURECA	European Retrievable Carrier launched (on space shuttle STS-46)
FOV	Field-of-view
FREESTAR	Fast Reaction Experiments Enabling Science and Technology Applications and Research
GUM	Guide to the expression of Uncertainty in Measurement
H-F	Hickey–Freidan, a family of cavity radiometers (thermopiles)
Hitchhiker	Not an acronym, an instrument package flown on the space shuttle
Hitchhiker/ FREESTAR	Flown on space shuttle STS-107 in January 2003
Hitchhiker/ IEH-03	Flown on space shuttle STS-95 in October 1998
Hitchhiker/ TAS-01	Flown on space shuttle STS-85 in August 1997
IEH-03	International Extreme ultraviolet Hitchhiker-03
ISS	International Space Station
JCGM	Joint Committee for Guides in Metrology
JPL	Jet Propulsion Laboratory
JPSS	Joint Polar Satellite System
LaRC	Langley Research Center
LASP	Laboratory for Atmospheric and Space Physics
METAS	Swiss Federal Office of Metrology
NASA	National Aeronautics and Space Administration
NIST	National Institute of Standards and Technology
NMI	National Metrology Institutes
NOAA	National Oceanic and Atmospheric Administration
NPL	National Physical Laboratory
PICARD	Not an acronym, a satellite mission named for Jean Picard
PMO6	Physikalisch-Meteorologisches Observatorium type 6 radiometer
PMOD/WRC	Physikalisch-Meteorologisches Observatorium Davos, World Radiation Center
POWR	Primary Optical Watt Radiometer
PREMOS	PREcision MOnitoring Sensor (on PICARD)
PSR	Primary Standard Radiometer
RMIB	Royal Meteorological Institute of Belgium
SIMBA	Solar Irradiance Monitoring by BAlloons experiment
SMD	Ministére des affaires économiques, service de métrologie
SMM	Solar Maximum Mission
SOHO	Solar and Heliospheric Observatory satellite
SOLCON	SOLar CONstant experiment (Spacelab, ATLAS, Hitchhiker)
SORCE	Solar Radiation and Climate Experiment
SOVA	SOlar VAriability experiment (EURECA)
SOVA-1	Instrument package containing DIARAD (SOVA/EURECA, Hitchhiker/TAS-01)
SOVA-2	Instrument package containing PMO6 (on EURECA)
SOVAP	SOlar VAriability PICARD experiment
SOVIM	SOlar Variability and Irradiance Monitor (on ISS)
Spacelab 1	Not an acronym, an instrument package flown on space shuttle STS-9 in November/December 1983
TAS-01	Technology Applications and Science-01
TCTE	TSI Calibration Transfer Experiment
TIM	Total Irradiance Monitor
TRF	TSI Radiometer Facility
TRW	Thompson Ramo Wooldridge, Inc.
TSI	Total Solar Irradiance
TSIS	Total Solar Irradiance Sensor
UARS	Upper Atmosphere Research Satellite
VIRGO	Variability of Irradiance and Gravity Oscillations experiment (on the SOHO satellite)
WRR	World Radiometric Reference

The authors are grateful to Dominique A. Crommelynck and Steven Dewitte of the Institut Royal Météorologique de Belgique, Brussels, Belgium; Claus Fröhlich and Wolfgang Finsterle of the Physikalisch-Meteorologisches Observatorium Davos/World Radiation Centre, Davos, Switzerland; Robert B. Lee III of the National Aeronautics and Space Administration, Langley Research Center, Hampton, Virginia, USA; Richard C. Willson of Columbia University, Coronado, California, USA; and Roger S. Helizon of the National Aeronautics and Space Administration, Jet Propulsion Laboratory, Pasadena, California, USA for submission of the comparison apertures, associated documentation, and useful discussions. Greg Kopp of the University of Colorado's LASP facility provided useful discussions. The comments and suggestions of the anonymous reviewers were helpful in finalizing the text. Vladimir Khromchenko and Curtis Suplee of

NIST provided technical assistance. The NASA EOS Project Science Office provided support (S 41365 F).

References and Notes

1. J. W. Harder, J. M. Fontenla, P. Pilewskie, E. C. Richard, and T. N. Woods, "Trends in solar spectral irradiance variability in the visible and infrared," Geophys. Res. Lett. **36**, L07801 (2009).
2. J. L. Lean, "The sun's variable radiation and its relevance for Earth," Annu. Rev. Astron. Astrophys. **35**, 33–67 (1997).
3. D. H. Rind, "The sun's role in climate variations," Science **296**, 673–677 (2002).
4. D. H. Rind, J. Lean, L. Lerner, P. Lonergan, and A. Leboissitier, "Exploring the stratospheric/tropospheric response to solar forcing," J. Geophys. Res. **113**, D24103 (2008).
5. J. L. Lean and D. H. Rind, "How natural and anthropogenic influences alter global and regional surface temperatures: 1889 to 2006," Geophys. Res. Lett. **35**, L18701 (2008).
6. J. L. Lean and D. H. Rind, "How will Earth's surface temperature change in future decades?" Geophys. Res. Lett. **36**, L15708 (2009).
7. G. B. Ohring, *Achieving Satellite Instrument Calibration for Climate Change (ASIC3), Center for Satellite Applications and Research* (NESDIS/NOAA, U.S. Dept. of Commerce, 2008).
8. G. Kopp, "Total Solar Irradiance Database" (2013), retrieved http://spot.colorado.edu/~koppg/TSI/TSI.jpg.
9. F. Hengstberger, *Absolute Radiometry: Electrically Calibrated Thermal Detectors of Optical Radiation* (Academic, 1989).
10. R. Goebel, M. Stock, and R. Köhler, "Report on the international comparison of cryogenic radiometers based on transfer detectors, Rapport BIPM-2000/9, September 2000" (Paris, France, 2000).
11. G. Kopp, K. Heuerman, D. Harber, and V. Drake, "The TSI radiometer facility—absolute calibrations for total solar irradiance instruments," Proc. SPIE **6677**, 667709 (2007).
12. C. Fröhlich and J. L. Lean, "The sun's total irradiance: cycles, trends and related climate change uncertainties since 1976," Geophys. Res. Lett. **25**, 4377–4380 (1998).
13. J. J. Butler, B. C. Johnson, J. P. Rice, E. L. Shirley, and R. A. Barnes, "Sources of differences in on-orbit total solar irradiance measurements," J. Res. Natl. Inst. Stand. Technol. **113**, 187–203 (2008).
14. G. M. Lawrence, G. Kopp, G. Rottman, J. Harder, T. Woods, and H. Loui, "Calibration of the total irradiance monitor," Metrologia **40**, S78–S80 (2003).
15. J. M. Houston and J. P. Rice, "NIST reference cryogenic radiometer designed for versatile performance," Metrologia **43**, S31–S35 (2006).
16. G. Kopp and J. L. Lean, "A new, lower value of total solar irradiance: evidence and climate significance," Geophys. Res. Lett. **38**, L01706 (2011).
17. J. J. Butler, "Calibration workshop for the total irradiance monitor (TIM) instrument on the Earth Observing System's (EOS) solar radiation and climate experiment," The Earth Observer **12**(3), 22–25 (2000).
18. J. J. Butler and B. C. Johnson, "Organization and implementation of calibration in the EOS project—part 1," The Earth Observer **8**(1), 22–27 (1996).
19. J. J. Butler and B. C. Johnson, "Calibration in the EOS project —part 2: implementation," The Earth Observer **8**(2), 26–31 (1996).
20. J. J. Butler and R. A. Barnes, "The use of transfer radiometers in validating the visible through shortwave infrared calibrations of radiance sources used by instruments in NASA's Earth Observing System," Metrologia **40**, S70–S77 (2003).
21. J. J. Butler, B. C. Johnson, J. P. Rice, S. W. Brown, and R. A. Barnes, "Validation of radiometric standards for laboratory calibration of reflected-solar Earth observing satellite instruments," Proc. SPIE **6677**, 667707 (2007).
22. E. A. Early, P. Y. Barnes, B. C. Johnson, J. J. Butler, C. J. Bruegge, S. F. Biggar, P. R. Spyak, and M. M. Pavlov, "Bidirectional reflectance round-robin in support of the Earth observing system program," J. Atmos. Ocean. Technol. **17**, 1077–1091 (2000).
23. J. B. Fowler, National Institute of Standards and Technology (personal communication, 2000).
24. B. C. Johnson, M. Litorja, and J. J. Butler, "Preliminary results of aperture area comparison for exo-atmospheric solar irradiance," Proc. SPIE **5151**, 454–462 (2003).
25. T. M. Goodman, J. E. Martin, B. D. Shipp, and N. P. Turner, "The manufacture and measurement of precision apertures," in *New Developments and Applications in Optical Radiometry*, N. P. Fox and D. H. Netttleton, eds., Vol. **92** of Institute of Physics Conference Series (Institute of Physics, 1989), pp. 121–128.
26. Roundness, a measure of radial deviations, is defined as the difference in radii of the two coplanar concentric circles that just include the profile of the surface.
27. J. E. Martin, N. P. Fox, N. J. Harrison, B. Shipp, and M. Anklin, "Determination and comparisons of aperture areas using geometric and radiometric techniques," Metrologia **35**, 461–464 (1998).
28. J. B. Fowler and G. Dezsi, "High-accuracy measurement of aperture area relative to standard known aperture," J. Res. NIST **100**, 277–283 (1995).
29. J. Hartmann, "Advanced comparator method for measuring ultra-small aperture areas," Meas. Sci. Technol. **12**, 1678–1682 (2001).
30. J. Fischer and M. Stock, "A noncontact measurement of radiometric apertures with an optical microtopography sensor," Meas. Sci. Technol. **3**, 693–698 (1992).
31. D. Crommelynck and S. Dewitte, "Metrology of total solar irradiance monitoring," Adv. Space Res. **24**, 195–204 (1999).
32. S. Mekaoui, S. Dewitte, D. Crommelynck, A. Chevalier, C. Conscience, and A. Joukoff, "Absolute accuracy and repeatability for the RMIB radiometers for TSI measurements," Sol. Phys. **224**, 237–246 (2004).
33. D. Crommelynck, "The observation of the solar irradiance and its variations, challenging space metrology," Sol. Phys. **74**, 509–519 (1981).
34. D. Crommelynck, "Fundamentals of absolute pyroheliometry and objective characterization," in *Langley Research Center Earth Radiation Science Seminars, NASA CP 2239*, J. B. Hall, ed. (NASA LaRC, 1982), pp. 53–88.
35. S. Dewitte, A. Joukoff, D. Crommelynck, R. B. Lee, R. Helizon, and R. S. Wilson, "Contribution of the Solar Constant (SOLCON) program to the long-term total solar irradiance observations," J. Geophys. Res. **106**, 15759–15765 (2001).
36. D. Crommelynck, R. W. Brusa, and V. Domingo, "Results of the solar constant experiment on board Spacelab 1," Sol. Phys. **107**, 1–9 (1986).
37. D. Crommelynck and V. Domingo, "Solar irradiance observations," Science **225**, 180–181 (1984).
38. D. Crommelynck, V. Domingo, B. R. Barkstrom, R. B. Lee, J. Donaldson, U. Telljohann, L. Warren, and A. Fichot, "Preliminary results of solar constant observations with the SOLCON experiment on ATLAS-1," Adv. Space Res. **14**, 253–262 (1994).
39. D. Crommelynck, A. Fichot, R. B. Lee, and J. Romero, "First realization of the space absolute radiometric reference (SARR) during the ATLAS 2 flight period," Adv. Space Res. **16**, 17–23 (1995).
40. D. Crommelynck, A. Fichot, V. Domingo, and R. B. Lee, "SOLCON solar constant observations from the ATLAS missions," Geophys. Res. Lett. **23**, 2293–2295 (1996).
41. D. Crommelynck, V. Domingo, A. Fichot, C. Fröhlich, B. Penelle, J. Romero, and C. Wehrli, "Preliminary results from the SOVA experiment on board the European Retrievable Carrier (EURECA)," Metrologia **30**, 375–379 (1993).
42. D. Crommelynck, V. Domingo, A. Fichot, and R. B. Lee, "Total solar irradiance observations from the EURECA and ATLAS missions," in *The Sun as a Variable Star: Solar and Stellar Irradiance Variations*, J. M. Pap, C. Fröhlich, H. S. Hudson, and S. K. Solanski, eds. (Cambridge University, 1994), pp. 63–69.
43. S. Mekaoui, S. Dewitte, C. Conscience, and A. Chevalier, "Total solar irradiance absolute level from DIARAD/SOVIM

on the international space station," Adv. Space Res. **45**, 1393–1406 (2010).
44. G. Schmidtke, C. Fröhlich, and G. Thuillier, "ISS-SOLAR: total (TSI) and spectral (SSI) irradiance measurements," Adv. Space Res. **37**, 255–264 (2006).
45. S. Dewitte, D. Crommelynck, and A. Joukoff, "Total solar irradiance observations from DIARAD/VIRGO," J. Geophys. Res. **109**, A02102 (2004).
46. C. Conscience, M. Meftah, A. Chevalier, S. Dewitte, and D. Crommelynck, "The space instrument SOVAP of the PICARD mission," Proc. SPIE **8146**, 814613 (2011).
47. G. Thuillier, S. Dewitte, and W. Schmutz, "Simultaneous measurement of the total solar irradiance and solar diameter by the PICARD mission," Adv. Space Res. **38**, 1792–1806 (2006).
48. L. Damé, D. Cugnet, M. Hersé, D. Crommelynck, S. Dewitte, A. Joukoff, I. Ruedi, W. Schmutz, C. Wehrli, C. Delmas, F. Laclare, and J.-P. Rozelot, "PICARD: Solar diameter, irradiance and climate," in *The Solar Cycle and Terrestrial Climate, Proceedings of the 1st Solar and Space Weather Euroconference*, A. Wilson, ed. (European Space Agency, 2000).
49. L. Damé, M. Hersé, G. Thuillier, T. Appourchaux, D. Crommelynck, S. Dewitte, A. Joukoff, C. Fröhlich, F. Laclare, C. Delmas, and P. Boumier, "PICARD: simultaneous measurements of the solar diameter, differential rotation, solar constant and their variations," Adv. Space Res. **24**, 205–214 (1999).
50. D. Crommelynck, "Factors limiting the accuracy of absolute radiometry," in *New Developments and Applications in Optical Radiometry*, N. P. Fox and D. H. Nettleton, eds., Vol. **92** of Institute of Physics Conference Series (Institute of Physics, 1989), pp. 19–25.
51. R. W. Brusa and C. Fröhlich, "Absolute radiometers (PMO6) and their experimental characterization," Appl. Opt. **25**, 4173–4180 (1986).
52. C. Fröhlich, "History of solar radiometry and the world radiometric reference," Metrologia **28**, 111–115 (1991).
53. C. Fröhlich, R. Philipona, J. Romero, and C. Wehrli, "Radiometry at the Physikalisch–Meteorologisches Observatorium Davos World Radiation Centre," Opt. Eng. **34**, 2757–2766 (1995).
54. C. Fröhlich and R. W. Brusa, "Solar radiation and its variation over time," Sol. Phys. **74**, 209–215 (1981).
55. R. C. Willson, H. S. Hudson, C. Fröhlich, and R. W. Brusa, "Long-term downward trend in total solar irradiance," Science **234**, 1114–1117 (1986).
56. J. Romero, C. Fröhlich, and C. Wehrli, "Solar total irradiance variability measured by SOVA-2 on board EURECA," Adv. Space Res. **16**, 29–32 (1995).
57. J. Romero, C. Wehrli, and C. Fröhlich, "Solar total irradiance variability from SOVA 2 on board EURECA," Sol. Phys. **152**, 23–29 (1994).
58. C. Fröhlich, "Solar irradiance variability since 1978, revision of the PMOD composite during solar cycle 21," Space Sci. Rev. **125**, 53–65 (2006).
59. C. Fröhlich and W. Finsterle, "Total solar irradiance from VIRGO on SOHO," in *The Solar Cycle and Terrestrial Climate, Proceedings of the 1st Solar and Space Weather Euroconference, ESA SP-463*, A. Wilson, ed. (European Space Agency, 2000), pp. 665–670.
60. C. Fröhlich, J. Romero, H. Roth, C. Wehrli, B. N. Andersen, T. Appourchaux, V. Domingo, U. Telljohann, G. Berthomieu, P. Delache, J. Provost, T. Toutain, D. Crommelynck, A. Chevalier, A. Fichot, W. Däppen, D. Gough, T. Hoeksema, A. Jiménez, M. F. Gómez, J. M. Herreros, T. R. Cortés, A. R. Jones, J. M. Pap, and R. C. Willson, "VIRGO: Experiment for helioseismology and solar irradiance monitoring," Sol. Phys. **162**, 101–128 (1995).
61. G. Thuillier, C. Fröhlich, and G. Schmidtke, "Spectral and total solar irradiance measurements on board the international space station," in *Proceedings of the 2nd European Symposium on the Utilisation of the International Space Station, ESA SP-433* (European Space Agency, 1999), pp. 605–611.
62. M. Anklin, C. Wehrli, C. Fröhlich, and F. Pepe, "Total solar and spectral irradiance measured in France during a stratospheric balloon flight," in *Fourteenth ESA Symposium on European Rocket and Balloon Programs and Related Research, ESA SP-437*, B. Kaldeich-Schürmann, ed. (European Space Agency, 1999), pp. 537–540.
63. J. E. Martin, N. P. Fox, and P. J. Key, "A cryogenic radiometer for absolute radiometric measurements," Metrologia **21**, 147–155 (1985).
64. J. Romero, N. P. Fox, and C. Fröhlich, "First comparison of the solar and an SI radiometric scale," Metrologia **28**, 125–128 (1991).
65. J. Romero, N. P. Fox, and C. Fröhlich, "Improved comparison of the world radiometric reference and the SI radiometric scale," Metrologia **32**, 523–524 (1995/96).
66. W. Finsterle, P. Blattner, S. Moebus, I. Rüedi, C. Wehrli, M. White, and W. Schmutz, "Third comparison of the world radiometric reference and the SI radiometric scale," Metrologia **45**, 377–381 (2008).
67. H. Jacobowitz, H. V. Soule, H. L. Kyle, and F. House, and Team, "Earth radiation budget (ERB) experiment: an overview," J. Geophys. Res. **89**, 5021–5038 (1984).
68. H. Jacobowitz, L. L. Stowe, and J. R. Hickey, "The Earth radiation budget (ERB) experiment," in *The Nimbus 7 Users' Guide*, C. R. Madrid, ed. (NASA GSFC, 1978), pp. 33–70.
69. J. R. Hickey and A. R. Karoli, "Radiometric calibrations for the Earth radiation budget experiment," Appl. Opt. **13**, 523–533 (1974).
70. J. R. Hickey, B. M. Alton, H. L. Kyle, and D. Hoyt, "Total solar irradiance measurements by ERB/Nimbus 7—a review of nine years," Space Sci. Rev. **48**, 321–342 (1988).
71. C. Fröhlich, "Long-term behavior of space radiometers," Metrologia **40**, S60–S65 (2003).
72. R. B. Lee and R. S. Wilson, "Validation of spacecraft active cavity radiometer total solar irradiance (TSI): long-term measurement trends using proxy TSI least squares analyses," Proc. SPIE **5570**, 352–362 (2004).
73. R. C. Willson, "Measurements of solar total irradiance and its variability," Space Sci. Rev. **38**, 203–242 (1984).
74. B. R. Barkstrom, "The Earth radiation budget experiment (ERBE)," Bull. Am. Meteorol. Soc. **65**, 1170–1185 (1984).
75. B. R. Barkstrom and G. L. Smith, "The Earth radiation budget experiment: science and implementation," Rev. Geophys. **24**, 379–390 (1986).
76. M. R. Luther, R. B. Lee, B. R. Barkstrom, J. E. Cooper, R. D. Cess, and C. H. Duncan, "Solar calibration results from two earth radiation budget experiment nonscanner instruments," Appl. Opt. **25**, 540–545 (1986).
77. R. B. Lee, B. R. Barkstrom, and R. D. Cess, "Characteristics of the Earth radiation budget experiment solar monitors," Appl. Opt. **26**, 3090–3096 (1987).
78. R. C. Willson, "Active cavity radiometric scale, international pyroheliometric scale, and solar constant," J. Geophys. Res. **76**, 4325–4340 (1971).
79. R. C. Willson, "New radiometric techniques and solar constant measurements," Sol. Energy **14**, 203–211 (1973).
80. R. C. Willson, "Active cavity radiometer," Appl. Opt. **12**, 810–817 (1973).
81. R. C. Willson, "Active cavity radiometer type IV," Appl. Opt. **18**, 179–188 (1979).
82. R. C. Willson, S. Gulkis, M. Janssen, H. S. Hudson, and G. A. Chapman, "Observations of solar irradiance variability," Science **211**, 700–702 (1981).
83. R. C. Willson and H. S. Hudson, "Solar maximum mission experiment: Initial observations by the active cavity radiometer," Adv. Space Res. **1**, 285–288 (1981).
84. R. C. Willson, "Active cavity radiometer type V," Appl. Opt. **19**, 3256–3257 (1980).
85. R. C. Willson, "Irradiance observations of SMM, Spacelab 1, UARS, and ATLAS missions," in *The Sun as a Variable Star: Solar and Stellar Irradiance Variations*, J. M. Pap, C. Fröhlich, H. S. Hudson, and S. K. Solanski, eds. (Cambridge University, 1994), pp. 54–62.
86. R. C. Willson and R. Helizon, "EOS/ACRIM III instrumentation," Proc. SPIE **3750**, 233–242 (1999).

87. R. C. Willson, "The ACRIMSAT/ACRIM III experiment—extending the precision, long-term total solar irradiance climate database," The Earth Observer **13**(3), 14–17 (2001).
88. M. Litorja, B. C. Johnson, and J. B. Fowler, "Area measurements of apertures for exo-atmospheric solar irradiance for JPL," Proc. SPIE **6677**, 667708 (2007).
89. J. B. Fowler, R. S. Durvasula, and A. C. Parr, "High-accuracy aperture-area measurement facilities at the National Institute of Standards and Technology," Metrologia **35**, 497–500 (1998).
90. J. B. Fowler and M. Litorja, "Geometric area measurements of circular apertures for radiometry at NIST," Metrologia **40**, S9–S12 (2003).
91. I. Kasa, "A circle fitting procedure and its error analysis," IEEE Trans. Instrum. Meas. **IM-25**, 8–14 (1976).
92. A. Albano, "Representation of digitized contours in terms of conic arcs and straight-line segments," Comput. Graph. Image Process. **3**, 23–33 (1974).
93. Type A uncertainty components are those evaluated using statistical analysis.
94. B. Efron and R. Tibshirani, *An Introduction to the Bootstrap, Monographs on Statistics and Applied Probability* (Chapman and Hall, 1993).
95. M. Litorja, J. B. Fowler, J. Hartmann, N. Fox, M. Stock, A. Razet, B. Khlevnoy, E. Ikonen, M. Machacs, and K. Doytchinov, "Final report on the CCPR-2 supplementary comparison of area measurements of apertures for radiometry," Metrologia **44**, 02002 (2007).
96. Evaluation of Measurement Data—Guide to the Expression of Uncertainty in Measurement, JCGM 100:2008 (Bureau International des Poids et Mesures, Paris, France, 2008).
97. An uncertainty for an 8 mm diameter aperture was stated to be equal to $u(d)$ at $k = 2$ plus twice the departure from roundness.
98. W. Finsterle, Physikalisch-Meteorologisches Observatorium Davos/World Radiation Center (personal communication, 2013).